

# Electronic structure and x-ray magnetic circular dichroism in Mn-doped topological insulators $\text{Bi}_2\text{Se}_3$ and $\text{Bi}_2\text{Te}_3$

V. N. Antonov,<sup>1,2,3</sup> L. V. Bekenov,<sup>1</sup> S. Uba,<sup>2</sup> and A. Ernst<sup>3,4</sup>

<sup>1</sup>*G. V. Kurdyumov Institute for Metal Physics of the N.A.S. of Ukraine, 36 Vernadsky Street, 03142 Kiev, Ukraine*

<sup>2</sup>*Faculty of Mathematics and Informatics, University of Białystok, K. Ciolkowskiego 1M, PL-15-245 Białystok, Poland*

<sup>3</sup>*Max-Planck Institut für Mikrostrukturphysik, Weinberg 2, D-06120 Halle, Germany*

<sup>4</sup>*Institut für Theoretische Physik, Johannes Kepler Universität, A 4040 Linz, Austria*

(Received 3 November 2017; revised manuscript received 1 December 2017; published 29 December 2017)

We studied the structural, electronic, and magnetic properties of Mn-doped topological insulators  $\text{Bi}_2\text{Se}_3$  and  $\text{Bi}_2\text{Te}_3$  within the density-functional theory (DFT) using the generalized gradient approximation (GGA) in the framework of the fully relativistic spin-polarized Dirac linear muffin-tin orbital band-structure method. The x-ray absorption spectra (XAS) and x-ray magnetic circular dichroism at the Mn  $K$  and  $L_{2,3}$  edges were investigated theoretically from first principles. The calculated results are in good agreement with experimental data. The complex fine structure of the Mn  $L_{2,3}$  XAS in Mn-doped  $\text{Bi}_2\text{Se}_3$  and  $\text{Bi}_2\text{Te}_3$  was found to be not compatible with a pure  $\text{Mn}^{3+}$  valency state. Its interpretation demands mixed valent states. The theoretically calculated x-ray emission spectra at the Mn  $K$  and  $L_{2,3}$  edges are also presented and analyzed.

DOI: [10.1103/PhysRevB.96.224434](https://doi.org/10.1103/PhysRevB.96.224434)

## I. INTRODUCTION

One of the most striking discoveries in recent years which has emerged from research into spin-orbit coupling is a new state of matter known as a topological insulator (TI) [1]. Topological insulators are fully gapped in the bulk but, due to strong spin-orbit coupling, possess metallic surface states which are protected by time-reversal symmetry (TRS). This results in the remarkable property that surface electrons cannot be backscattered, i.e., they are robust against perturbations [2] as long as those perturbations, e.g., in the form of doping or surface adatoms, are nonmagnetic. The band structure calculations [3] and angle-resolved photoemission spectroscopy (ARPES) measurements [4,5] indicate that  $\text{Bi}_2\text{Se}_3$ ,  $\text{Bi}_2\text{Te}_3$  and several related layered compounds exhibit a single Dirac cone on the Fermi surface with linear dispersion around the  $\Gamma$  point, a hallmark of a topological insulator. Typically, the Dirac point (DP), the tip of the cone, is located a few hundred meV below the Fermi energy  $E_F$  and the bulk conduction band crosses  $E_F$  [4,6,7]. Such a situation makes it difficult to observe the signals from Dirac fermions by transport experiments. Beyond the inherent importance of exploring a complex phase of quantum matter, these systems are of great interest for device applications involving quantum computing [8] and photonics [9]. Current research on these materials is developing rapidly (see Review articles [10–14]).

Three-dimensional (3D) TIs offer nontrivial surface states that can be utilized to perform dissipationless spin transport. However, it is also important to break the TRS of TIs to realize novel physical phenomena such as, for example, the carrier-independent long-range ferromagnetic order [15], giant magneto-optical Kerr effect [16] or the newly discovered quantum anomalous Hall effect (QAHE) [17,18]. The QAHE observed in magnetic TIs where quantized transport occurs in the absence of an external magnetic field and thus discrete Landau levels. The key ingredient for observing the QAHE is the opening of a band gap in the band structure of the topological surface state at the Dirac point. It can be achieved by applying a magnetic field or inducing ferromagnetism

in the TI. Ferromagnetic ordering has been successfully achieved in 3D  $(\text{Bi,Sb})_2(\text{Se,Te})_3$  type TIs by doping with 3d transition metals, such as Cr, V, and Mn [19–24]. Indeed, the QAH effect has been reported in the Cr-doped  $(\text{Bi,Sb})_2\text{Te}_3$  system [17,25,26]. Among the various transition metal atoms, V-doped  $\text{Sb}_2\text{Te}_2$  exhibits the most stable ferromagnetism, with a high Curie temperature [20,27,28].

Despite the intensive research on TM-doped  $\text{Bi}_2(\text{Se,Te})_3$  type TIs, the interpretations for the observed ferromagnetic (FM) properties have often been controversial. For spintronic applications, the ferromagnetism in a semiconductor needs to be intrinsic, that is, not from magnetic clusters of the doped transition-metal impurities. Some studies suggest that the FM in TM-doped TIs originates from the presence of secondary phases or FM clusters, whereas other results indicate the existence of intrinsic FM of TM substitution in the  $\text{Bi}_2(\text{Se,Te})_3$  lattice. Also, a number of recent studies showed that the observed ferromagnetism tends to depend on methods and conditions used in the sample preparation. Thus no consensus on the proper origin of the ferromagnetism in such doped TIs has been reached yet. Therefore more intensive and extensive study is essential.

Collins-McIntyre *et al.* [22] have demonstrated the high-quality molecular beam epitaxy (MBE) growth of Mn-doped  $\text{Bi}_2\text{Se}_3$  thin films. It was found that Mn dopants may be introduced into the host  $\text{Bi}_2\text{Se}_3$  without the formation of additional parasitic phases or significant degradation to the host crystal structure up to a doping concentration of  $\sim 7.5$  at. % Mn. From the compositional analysis by Rutherford backscattering spectrometry (RBS), it is apparent that Mn is incorporated substitutionally for low doping concentrations, before also being incorporated interstitially (in the van der Waals gap between the layers) at higher doping concentrations. A saturation magnetization of  $5.1 \mu_B/\text{Mn}$  is obtained from SQUID magnetometry, pointing towards a Mn valency of  $2+$ . However, a much lower moment of  $1.6 \mu_B/\text{Mn}$  was revealed from surface-sensitive XMCD measurements. Authors conclude that the exact nature in which Mn dopants incorporate in the host  $\text{Bi}_2\text{Se}_3$  crystal is still unresolved.

Watson *et al.* reports a study of Mn-doped  $\text{Bi}_2\text{Te}_3$  single crystals with nominal Mn concentrations of  $x = 0.09$  and  $0.15$  with a ferromagnetic transition temperature of  $\sim 9\text{--}13$  K [29]. SQUID magnetometry measurements on  $x = 0.15$  crystals show that the samples are soft ferromagnets with small coercive fields with a saturation magnetic moment of  $4.4(5) \mu_B$  per Mn atom reached at  $\sim 1.5$  T [29]. It is between the expected value for the  $\text{Mn}^{3+}$  ( $4 \mu_B$ ) and  $\text{Mn}^{2+}$  ( $5 \mu_B$ ). It is consistent with previous calculations which give  $4 \mu_B$  [30] and  $4.5 \mu_B$  [31], respectively, but disagrees with the theoretical predictions by Larson and Lambrecht [32] and by Zhang *et al.* [33] who calculated a Mn valency of  $3+$  in  $\text{Bi}_2\text{Se}_3$  and  $\text{Bi}_2\text{Te}_3$ . Watson *et al.* [29] also measured x-ray magnetic circular dichroism (XMCD) in Mn-doped  $\text{Bi}_2\text{Te}_3$  at the Mn  $L_{2,3}$  edges at  $1.8$  K in the total-electron-yield (TEY) mode, which is surface sensitive (with an exponentially decaying sampling depth of  $3\text{--}5$  nm). The results indicate a ground state of mixed  $d^4\text{--}d^5\text{--}d^6$  character of a localized electronic nature. The orbital magnetic moment on Mn of  $0.18 \mu_B$  is small (4% of the total Mn moment), as obtained by the sum-rule analysis of the Mn XMCD in a saturated field at  $1.8$  K. The multiplet calculations of the XAS and XMCD Mn  $L_{2,3}$  spectra were performed using the Anderson impurity-model for a mixed ground state of 16%  $d^4$ , 58%  $d^5$ , and 26%  $d^6$  character, which gives as average a total  $3d$  count of  $5.1$ . Sessi *et al.* [34] also measured the XAS and XMCD spectra at the Mn  $L_{2,3}$  edges of Mn-doped  $\text{Bi}_2\text{Te}_3$ , obtained at normal and grazing incidence, with an external magnetic field  $B = 6$  T and  $T = 2.5$  K. They provide density-functional-theory calculations based on the local density approximation in the frame of the Korringa-Kohn-Rostoker (KKR) Green-function method for the calculation of the impurity electronic structure and scattering properties ( $T$  matrix and surface-state scattering rate). The  $\text{Bi}_2\text{Te}_3$  surface was modeled by a six-quintuple layer film. The x-ray magnetic circular dichroism shows superparamagnetism even at very dilute Mn concentrations.

Here we present theoretical calculations of the XAS and XMCD spectra of Mn-doped  $\text{Bi}_2(\text{Se},\text{Te})_3$  from first principles. We found that the complex fine structure of the Mn  $L_{2,3}$  XAS in Mn-doped  $\text{Bi}_2(\text{Se},\text{Te})_3$  is not compatible with a pure  $\text{Mn}^{3+}$  valency state. Its interpretation demands mixed valent states. The energy band structure of Mn-doped  $\text{Bi}_2(\text{Se},\text{Te})_3$  compounds in this paper is calculated within the *ab initio* approach by applying the generalized gradient approximation (GGA) using the fully relativistic spin-polarized Dirac linear muffin-tin orbital band-structure method. The paper is organized as follows. The computational details are presented in Sec. II. Section III presents the electronic structure of Mn-doped  $\text{Bi}_2(\text{Se},\text{Te})_3$  compounds. Section IV presents the XAS and XMCD spectra of Mn-doped  $\text{Bi}_2(\text{Se},\text{Te})_3$  compounds. Theoretical results are compared with experimental measurements. Finally, the results are summarized in Sec. V.

## II. COMPUTATIONAL DETAILS

*a. Crystal structure.*  $\text{Bi}_2\text{Se}_3$  was synthesized in late 1950s [35]. Since that time a rich body of theoretical and experimental work has grown out of the effort to explain and exploit the large thermoelectric effect which the material exhibits [36].

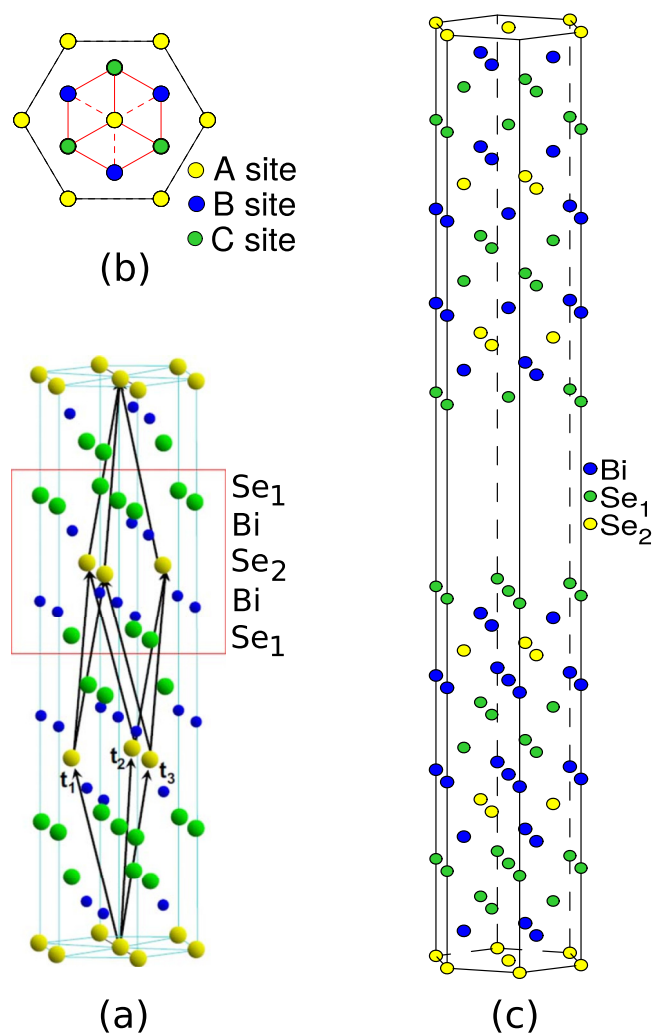


FIG. 1. Crystal structure of the  $\text{Bi}_2\text{Se}_3$  compound. (a) The hexagonal supercell containing 15 atomic layers. The quintuple layer is shown in the red box. (b) The top view of a QL in the triangle lattice. Three sets of different sites, labeled as A, B, and C sublattices, respectively, are presented. Owing to the  $D_{3d}^5$  symmetry, the stacking of atomic layers along the  $z$  direction is in the order of  $\dots\text{C}(\text{Se}_1)\text{--A}(\text{Bi})\text{--B}(\text{Se}_2)\text{--C}(\text{Bi})\text{--A}(\text{Se}_1)\text{--B}(\text{Se}_1)\text{--C}(\text{Bi})\text{--A}(\text{Se}_2)\text{--}\dots$  (c) Crystal structure of the  $\text{Bi}_2\text{Se}_3$  (111) thin film with the thickness of six quintuple layers with one quintuple replaced by empty spheres.

$\text{Bi}_2\text{Se}_3$  is a narrow band gap semiconductor with a tetradymite crystal structure with the space group  $D_{3d}^5 (R\bar{3}m)$ , number 166. This rhombohedral layered structure is formed by five atomic layers as a basic unit cell, named a quintuple layer (QL) [see Fig. 1(a)]. The interlayer bonding within the QLs are strong because of the dominant covalent character, but the bonding between the QLs is much weaker due to the van der Waals-type interaction. The same structure is common to other narrow band gap semiconductor chalcogenides, like  $\text{Bi}_2\text{Te}_3$  and  $\text{Sb}_2\text{Te}_3$ . There are two equivalent Se atoms ( $\text{Se}_1$ ), two equivalent Bi atoms, and one Se atom ( $\text{Se}_2$ ), which is inequivalent to the  $\text{Se}_1$  atoms. Our coordinate system is set as follows: the origin is set at the  $\text{Se}_2$  site; the  $z$  direction is set perpendicular to the atomic layer, the  $x$  direction is taken along

the binary axis with the twofold rotation symmetry, and the  $y$  direction is taken along the bisectrix axis, which is the crossing line of the reflection plane and the  $\text{Se}_2$  atomic layer plane.

*b. X-ray magnetic circular dichroism.* Magneto-optical (MO) effects refer to various changes in the polarization state of light upon interaction with materials possessing a net magnetic moment, including rotation of the plane of linearly polarized light (Faraday, Kerr rotation), and the complementary differential absorption of left and right circularly polarized light (circular dichroism). In the near visible spectral range, these effects result from excitation of electrons in the conduction band. Near x-ray absorption edges, or resonances, magneto-optical effects can be enhanced by transitions from well-defined atomic core levels to transition symmetry selected valence states.

Within the one-particle approximation, the absorption coefficient  $\mu_\lambda^j(\omega)$  for incident x-ray of polarization  $\lambda$  and photon energy  $\hbar\omega$  can be determined as the probability of electronic transitions from initial core states with the total angular momentum  $j$  to final unoccupied Bloch states

$$\mu_\lambda^j(\omega) = \sum_{m_j} \sum_{n\mathbf{k}} |\langle \Psi_{n\mathbf{k}} | \Pi_\lambda | \Psi_{jm_j} \rangle|^2 \delta(E_{n\mathbf{k}} - E_{jm_j} - \hbar\omega) \times \theta(E_{n\mathbf{k}} - E_F), \quad (1)$$

where  $\Psi_{jm_j}$  and  $E_{jm_j}$  are the wave function and the energy of a core state with the projection of the total angular momentum  $m_j$ ;  $\Psi_{n\mathbf{k}}$  and  $E_{n\mathbf{k}}$  are the wave function and the energy of a valence state in the  $n$ th band with the wave vector  $\mathbf{k}$ ;  $E_F$  is the Fermi energy.

$\Pi_\lambda$  is the electron-photon interaction operator in the dipole approximation

$$\Pi_\lambda = -e\alpha\mathbf{a}_\lambda, \quad (2)$$

where  $\alpha$  are the Dirac matrices,  $\mathbf{a}_\lambda$  is the  $\lambda$  polarization unit vector of the photon vector potential, with  $a_\pm = 1/\sqrt{2}(1, \pm i, 0)$ ,  $a_\parallel = (0, 0, 1)$ . Here,  $+$  and  $-$  denotes, respectively, left and right circular photon polarizations with respect to the magnetization direction in the solid. Then, x-ray magnetic circular and linear dichroism are given by  $\mu_+ - \mu_-$  and  $\mu_\parallel - (\mu_+ + \mu_-)/2$ , respectively. More detailed expressions of the matrix elements in the electric dipole approximation may be found in Refs. [37–40]. The matrix elements due to magnetic dipole and electric quadrupole corrections are presented in Ref. [40].

Concurrent with the development of the x-ray magnetic circular dichroism experiment, some important magneto-optical sum rules have been derived [41–46]. For the  $L_{2,3}$  edges the  $l_z$  sum rule can be written as [39]

$$\langle l_z \rangle = n_h \frac{4}{3} \frac{\int_{L_3+L_2} d\omega(\mu_+ - \mu_-)}{\int_{L_3+L_2} d\omega(\mu_+ + \mu_-)}, \quad (3)$$

where  $n_h$  is the number of holes in the  $d$  band  $n_h = 10 - n_d$ ,  $\langle l_z \rangle$  is the average of the magnetic quantum number of the orbital angular momentum. The integration is taken over the

whole  $2p$  absorption region. The  $s_z$  sum rule can be written as

$$\langle s_z \rangle + \frac{7}{2} \langle t_z \rangle = n_h \frac{\int_{L_3} d\omega(\mu_+ - \mu_-) - 2 \int_{L_2} d\omega(\mu_+ - \mu_-)}{\int_{L_3+L_2} d\omega(\mu_+ + \mu_-)}, \quad (4)$$

where  $t_z$  is the  $z$  component of the magnetic dipole operator  $\mathbf{t} = \mathbf{s} - 3\mathbf{r}(\mathbf{r} \cdot \mathbf{s})/|\mathbf{r}|^2$ , which accounts for the asphericity of the spin moment. The integration  $\int_{L_3}$  ( $\int_{L_2}$ ) is taken only over the  $2p_{3/2}$  ( $2p_{1/2}$ ) absorption region.

*c. Calculation details.* The details of the computational method are described in our previous papers [47–50], and here we only mention several aspects. Band structure calculations were performed using the fully relativistic linear muffin-tin orbital (LMTO) method [51,52]. This implementation of the LMTO method uses four-component basis functions constructed by solving the Dirac equation inside an atomic sphere [53], which is crucial for a correct description of  $p_{1/2}$  states of heavy elements such as Pb or Bi [54]. The exchange-correlation functional of a GGA-type was used in the version of Perdew, Burke and Ernzerhof (PBE) [55,56]. Brillouin zone (BZ) integrations were performed using the improved tetrahedron method [57]. The basis consisted of Mn  $s$ ,  $p$ , and  $d$ , and Bi, Se, and Te  $s$ ,  $p$ , and  $d$  LMTO's.

The electronic structure of surface states was investigated for crystal structure of the  $\text{Bi}_2(\text{Se}, \text{Te})_3$  (111) thin film with the thickness of six QLs with one quintuple replaced by empty spheres [see Fig. 1(c)]. The interlayer bonding between two QLs is much weaker than that inside the QL; it is natural to expect that the cleavage plane should be between two QLs. This fact has been well confirmed by recent experiments on the layer-by-layer MBE growth of ultrathin film [58]. We therefore focus on this type of surface termination [with  $\text{Se}_1$  ( $\text{Te}_1$ ) atomic layer as the top most layer in Fig. 1(c)].

To investigate the electronic and magnetic properties of bulk  $\text{Bi}_2(\text{Se}, \text{Te})_3$  with dilute Mn doping, a  $(2 \times 2 \times 1)$  supercell containing 24 Bi and 36 Se(Te) atoms was employed. We use the experimental lattice constants  $a = 4.138 \text{ \AA}$  and  $c = 28.640 \text{ \AA}$  with internal parameters  $\nu = 0.206$  and  $\mu = 0.399$  for  $\text{Bi}_2\text{Se}_3$  [59] and  $a = 4.3847 \text{ \AA}$ ,  $c = 30.4984 \text{ \AA}$  with internal parameters  $\nu = 0.2115$  and  $\mu = 0.3985$  for  $\text{Bi}_2\text{Te}_3$  [60]. The layered crystal structure of  $\text{Bi}_2\text{Se}_3$  and  $\text{Bi}_2\text{Te}_3$  materials allows the transition metal dopants not only to enter the host substitutionally but also interstitially in the van der Waals gap between the layers. Therefore we produce two types of calculations with an Mn-doped atom substituting for Bi atoms with a dopant concentration of 4.17 at. % ( $x = 0.0417$ ) and with an additional Mn in the van der Waals gap between the QLs. In the latter case, a dopant concentration is equal to 8.34 at. % ( $x = 0.0834$ ). Thus the dopant concentration is 4.17 at. % ( $x = 0.0417$ ) for single substituted Mn and 8.34 at. % with an additional Mn in the der Waals gap. The concentrations are comparable to 7.5 at. % in the Mn-doped  $\text{Bi}_2\text{Se}_3$  used by Collins-McIntyre *et al.* [22], 9 at. % in  $\text{Bi}_2\text{Te}_3$  in the measurements by Vobornik *et al.* [61], 9 at. % of doped Mn ions in  $\text{Bi}_2\text{Te}_3$  used by Watson *et al.* [29], and 0.016 ML in  $\text{Bi}_2\text{Te}_3$  [34]. We take into account the lattice relaxation of  $\text{Bi}_2(\text{Se}, \text{Te})_3$  crystals with Mn-doping using the Vienna *ab initio* simulation package (VASP) [56,62,63].

The x-ray absorption and dichroism spectra were calculated taking into account the exchange splitting of core levels. The finite lifetime of a core hole was accounted for by folding the spectra with a Lorentzian. The widths of core level spectra  $\Gamma_{L_{2,3}}$  for Mn were taken from Ref. [64]. The finite apparatus resolution of the spectrometer was accounted for by a Gaussian of width 0.6 eV.

In the x-ray absorption process, an electron is promoted from a core level to an unoccupied state, leaving a core hole. As a result, the electronic structure at this state differs from that of the ground state. In order to reproduce the experimental spectrum, self-consistent calculations should be carried out including a core hole. In early calculations of the XAS spectra to account for the core-hole relaxation, a popular approach in conjunction with a large-cluster molecular-orbital calculation was the so-called Slater's transition state [65,66]. The XAS spectrum is represented by the corresponding partial DOS of a transition state in which the core state of the central atom has only a 1/2 electron occupation, with the other 1/2 electron placed at the lowest unoccupied molecular orbitals [66,67]. The calculation for Slater's transition state is a useful way to compute the difference in total energies between initial and final states, i.e., the absolute transition energy. However, it does not mean that the core-hole effects to change the energies and spatial distribution of wave functions are best reproduced by the calculation for the transition state. Strictly speaking, the core-hole effect is a two-particle interaction between an electron in the unoccupied conduction band and a hole in the core. Their interaction must be accounted for, and separate calculations of the initial and final states are necessary.

An alternative approach to account for the core-hole effect is the  $Z + 1$  approximation in which the core-hole effects are introduced by increasing the atomic number ( $Z$ ) by 1. Lie *et al.* succeeded in the reproduction of B  $K$  XAS from  $\text{AlB}_2$  and  $\text{TiB}_2$  using the  $Z + 1$  approximation [68,69]. But, one must realize that the  $Z + 1$  approximation is not always appropriate [70]. Nufer *et al.* reported the theoretical calculation of Al  $K$  and Al  $L_1$  XAS of  $\text{Al}_2\text{O}_3$  using the  $Z + 1$  approximation [71]. They demonstrated that this approximation is not applicable to the  $L_1$  edge. Even when the spectrum accidentally reproduces the experimental spectrum, estimation of the absolute transition energy is impossible by the  $Z + 1$  approximation.

In this study, the core-hole effect was fully taken into account in the self-consistent iterations by removing an electron at the core orbital using the supercell approximation. The core state of the target atom in the ground state provides the initial state  $|i\rangle$  for the spectral calculation. The final states  $|f\rangle$  are the conduction band states obtained separately by calculations in which one of the core electrons of the target atom is placed at the lowest conduction band. The interaction and the screening of the electron-hole pair are fully accounted for by the self-consistent iterations of the final state Kohn-Sham equations. This procedure simulates the experimental situation, in which the sample can easily supply an electron to screen a localized charge produced by the core hole. Such an approach allows for the symmetry breaking of the system in a natural way, and self-consistently describes the charge redistribution induced by the core hole. A similar approximation has been used by several authors [69,70,72–75]. We should mention that the size of the supercell

is important, and ultimately it should be large enough to inhibit interaction between excited atoms in neighboring supercells. In our calculations, we used a  $2 \times 2 \times 2$  supercell. At one of the four Mn atoms we create a hole at the  $2p_{1/2}$  or  $2p_{3/2}$  levels separately for the self-consistent GGA calculations of the  $L_2$  and  $L_3$  spectra, respectively.

### III. ELECTRONIC STRUCTURE

#### A. The linear dispersion of surface states

Figure 2 presents the *ab initio* calculated band structure of the  $\text{Bi}_2\text{Se}_3$  and  $\text{Bi}_2\text{Te}_3$  (111) thin films with the thickness of six quintuple layers for nonrelativistic (upper row) and fully relativistic Dirac (lower row) approximations. The surface states are indicated by red lines while the other lines correspond to the bulk bands. The nonrelativistic calculations produce a rather large energy band gap at the Fermi level of around 0.544 eV and 0.543 eV for  $\text{Bi}_2\text{Se}_3$  and  $\text{Bi}_2\text{Te}_3$ , respectively. In the fully relativistic Dirac approximation [Fig. 2 (lower row)], two chiral surface states are clearly seen which connect the conduction and valence bands forming a single Dirac-type contact at the  $\Gamma$  point aligned with the Fermi energy. Our calculations are in good agreement with previous calculations [76–80]. The Dirac point of  $\text{Bi}_2\text{Se}_3$  in our calculations as well as in other theoretical calculations is located relatively closer to the Fermi level than the position derived from ARPES measurements because the measurements took place for  $\text{Bi}_2\text{Se}_3$  samples which are typically electron doped by inner point defects [81–83]. There is a crucial detail that distinguishes  $\text{Bi}_2\text{Te}_3$  from  $\text{Bi}_2\text{Se}_3$ : in  $\text{Bi}_2\text{Se}_3$  the DP is located a few hundred meV below the Fermi energy  $E_F$ , however, the DP of  $\text{Bi}_2\text{Te}_3$  is situated deeply below the  $E_F$  and the valence-band maximum.

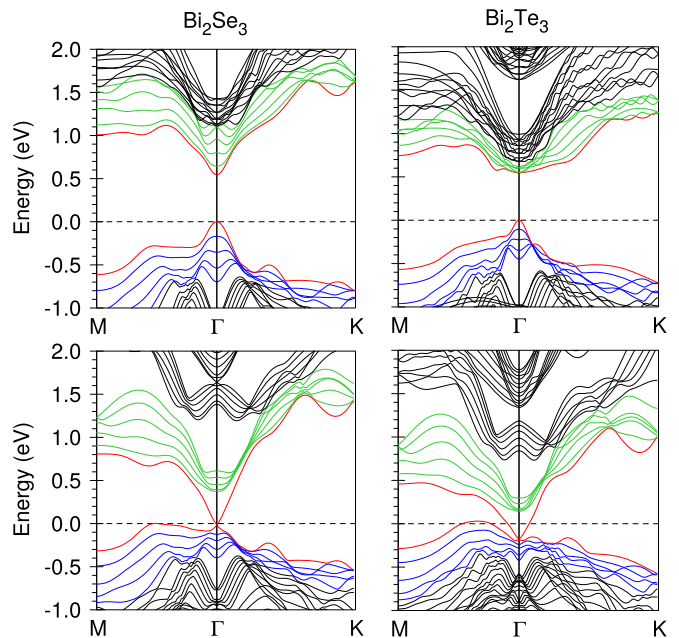


FIG. 2. The *ab initio* calculated band structure of the  $\text{Bi}_2\text{Se}_3$  (left) and  $\text{Bi}_2\text{Te}_3$  (right) (111) thin films with the thickness of six quintuple layers for nonrelativistic (upper row) and fully relativistic Dirac (lower row) approximations; the red lines indicate the surface states while the other lines correspond to the bulk bands.

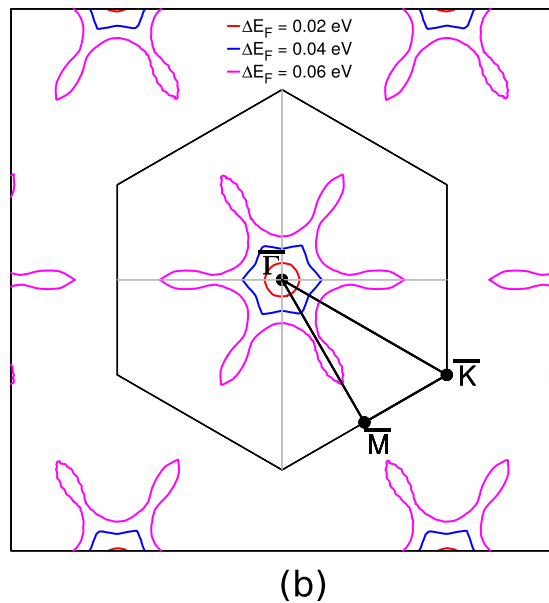
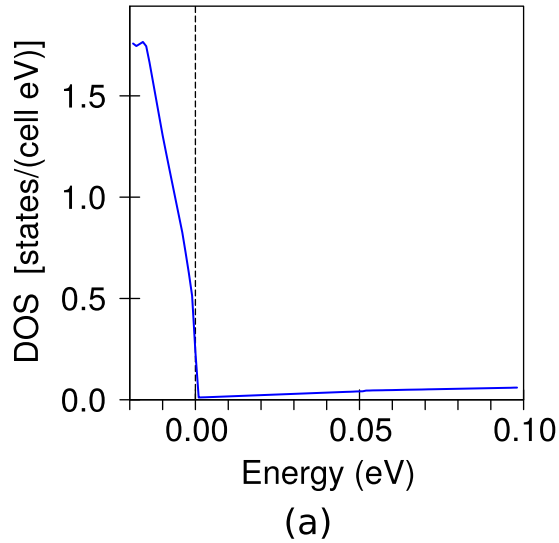


FIG. 3. (a) The total DOS in the close vicinity of the Fermi level for a five-QL slab of  $\text{Bi}_2\text{Se}_3$  (111) in the fully relativistic Dirac approximation. The DOS near the Fermi level is highly linear to energy due to the presence of Dirac cone-type surface states. (b) The hexagonal warping of cross sections of Dirac cone near the Fermi level in the plane perpendicular to the  $z$  direction for  $\Delta E_F = 0.02$  (red curves),  $0.04$  (blue curves), and  $0.06$  eV (magenta curves) in the fully relativistic Dirac approximation.

The gapless surface states that connect the bulk valence and conduction bands have almost linear energy dependence near the Dirac point. A linear band structure in 2D should lead to linear density of states (DOS). To be specific, in the bulk energy gap the energy bands are mostly from the surface states, so the DOS in the bulk energy gap are expected to be highly linear. Indeed, the corresponding DOS of  $\text{Bi}_2\text{Se}_3$  [presented in Fig. 3(a)] shows very good linear energy dependence within the bulk energy gap, as expected. This type of DOS can be easily measured by low-temperature scanning tunneling spectroscopy, which will provide an indirect method to probe the existence of linear surface states.

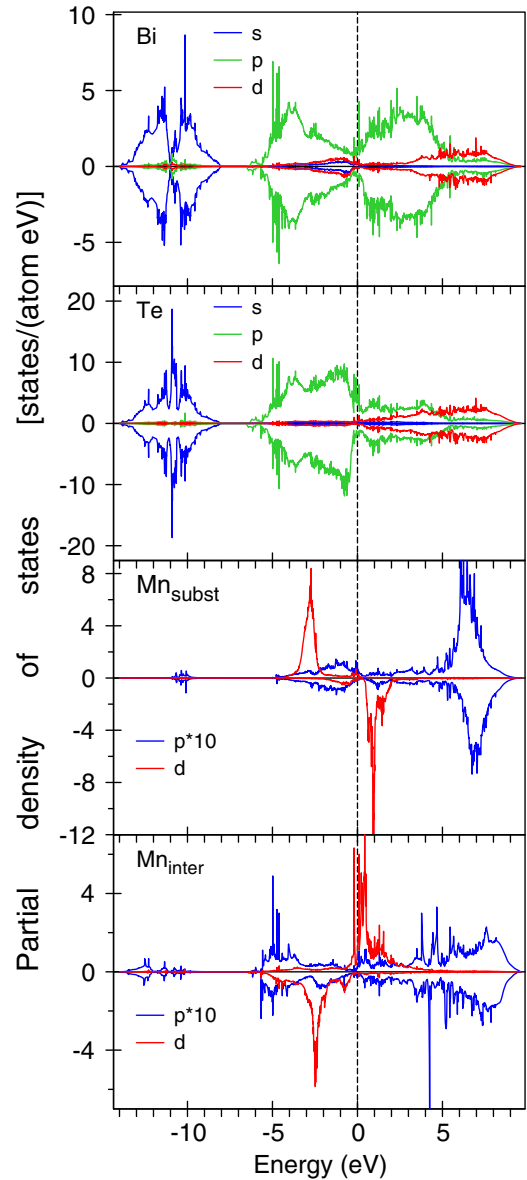


FIG. 4. The partial DOSs of bulk  $\text{Mn}_x\text{Bi}_{2-x}\text{Te}_3$  ( $x = 0.0834$ ) with one Bi atom substituted by a  $\text{Mn}_{\text{subst}}$  atom, and another  $\text{Mn}_{\text{inter}}$  atom in the van der Waals gap. The Mn  $4p$  PDOSs are multiplied by a factor of 10.

Figure 3(b) presents the calculated in the fully relativistic Dirac approximation hexagonal warping of cross sections of Dirac cone in  $\text{Bi}_2\text{Se}_3$  near the Fermi level in the plane perpendicular to the  $z$  direction for  $\Delta E_F = 0.02$  (red curves),  $0.04$  (blue curves), and  $0.06$  eV (green curves). When the Fermi level is close to the Dirac point the corresponding Fermi surface is nearly a perfect circle, while if the Fermi level is away from the Dirac point the properties of the surface states are significantly affected by the bulk states and thus satisfy the crystal symmetry. The Fermi surface becomes hexagonlike satisfying the  $C_{3v}$  crystal symmetry.

### B. Mn-substituted 3D energy band structure

Figure 4 presents the total and partial density of states for a 60-atom  $\text{Bi}_2\text{Te}_3$  unit cell containing one Mn substitutional

and one Mn atom in the van der Waals gap between the layers ( $x = 0.0834$ ). From total energy calculations we found that there is an antiferromagnetic arrangement of the Mn moments. The Bi  $6s$  and Te  $5s$  states are located mostly between  $-14.1$  and  $-8$  eV below the Fermi level and the  $p$  states of the Bi and Te are found from  $-6.9$  to  $9.2$  eV. There is an energy gap between Bi and Te  $s$  and  $p$  valent states of around 1 eV. The spin splitting of the Bi and Te  $p$  states is quite small.

The substitutional  $\text{Mn}_{\text{subst}}$  atom at the Bi site has three Te nearest-neighbor atoms at the distance of  $3.0652$  Å, three Te atoms at  $3.2185$  Å, and three Bi atoms at  $4.7126$  Å. The lattice relaxation decreases the  $\text{Mn}_{\text{subst}} - \text{Te}$  interatomic distances by  $0.115$  and  $0.082$  Å for the first and second groups of the Te atoms, respectively. The interstitial  $\text{Mn}_{\text{inter}}$  atom in the van der Waals gap has six Te atoms at the distance of  $2.8772$  Å and two Bi atoms at  $3.0956$  Å. The lattice relaxation increases the  $\text{Mn}_{\text{inter}} - \text{Te}$  distance by  $0.054$  Å and  $\text{Mn}_{\text{inter}} - \text{Bi}$  distance by  $0.105$  Å. The  $\text{Mn}_{\text{subst}}$   $3d$  impurity valence states consist of a single rather narrow peak at around  $-3$  eV, a conduction band peak is situated at 1 eV above the Fermi level. The  $\text{Mn}_{\text{inter}}$   $3d$  states are slightly wider and more structured in comparison with the corresponding  $3d$  states of substitutional  $\text{Mn}_{\text{subst}}$  ions. There is also a narrow  $3d$  peak in the close vicinity of the Fermi energy at  $-0.2$  eV for the  $\text{Mn}_{\text{inter}}$  ions. The crystal field at the  $\text{Mn}_{\text{subst}}$  and  $\text{Mn}_{\text{inter}}$  sites ( $C_{3v}$  point symmetry) causes the splitting of Mn  $d$  orbitals into a singlet  $a_1$  ( $d_{3z^2-1}$ ) and two doublets  $e$  ( $d_{yz}$  and  $d_{xz}$ ) and  $e_1$  ( $d_{xy}$  and  $d_{x^2-y^2}$ ). The major peak of  $\text{Mn}_{\text{subst}}$   $3d$  valence states at  $-3$  eV is formed by almost equal proportion of the  $a_1$ ,  $e$ , and  $e_2$  states. The corresponding peak in the  $\text{Mn}_{\text{inter}}$   $3d$  valence states at  $-2.5$  eV is mostly due to the  $e_1$  ( $d_{xy}$  and  $d_{x^2-y^2}$ ) states. The narrow  $3d$  peak in the close vicinity of the Fermi energy at  $-0.2$  eV for the  $\text{Mn}_{\text{inter}}$  ions is mostly formed by the  $a_1$  ( $d_{3z^2-1}$ ) states. The empty spin down  $\text{Mn}_{\text{subst}}$   $3d$  states at 1 eV above the Fermi energy are of  $e_1$  symmetry.

Our band structure calculations yield the spin magnetic moment  $M_s = 4.398 \mu_B$  and orbital magnetic moment  $M_l$  of  $0.072 \mu_B$  for the substitutional  $\text{Mn}_{\text{subst}}$  ions. The corresponding magnetic moments for the interstitial  $\text{Mn}_{\text{inter}}$  ions in the van der Waals gap are equal to  $M_s = -3.640 \mu_B$  and  $M_l = -0.095 \mu_B$ . Therefore the valencies were found to be equal to  $2.5+$  ( $d^{4.5}$ ) and  $1.7+$  ( $d^{5.3}$ ) for the  $\text{Mn}_{\text{subst}}$  and  $\text{Mn}_{\text{inter}}$  ions, respectively. We obtained smaller orbital magnetic moments at the Mn sites in comparison with experimental results of  $0.18 \mu_B$  estimated by Watson *et al.* using the sum-rule analysis of the Mn XMCD at the Mn  $L_{2,3}$  edges in the total-electron-yield mode [29]. The average induced spin magnetic moments at the Bi and Te sites are  $0.005 \mu_B$  and  $-0.008 \mu_B$ , respectively, with substitutional Mn ions only. If the system contains both the substitutional and interstitial Mn ions the average induced spin magnetic moments at the Bi and Te sites slightly increase and become equal to  $0.007 \mu_B$ , and  $-0.012 \mu_B$ , respectively. The orbital moments at the Bi and Te sites are very small (in the order of  $10^{-3} \mu_B$ ).

## IV. X-RAY ABSORPTION AND EMISSION SPECTRA

### A. Mn $L_{2,3}$ XAS and XMCD spectra

The XAS and the XMCD spectra at the Mn  $L_{2,3}$  edges in the Mn doped  $\text{Bi}_2\text{Te}_3$  and  $\text{Bi}_2\text{Se}_3$  TIs were measured by

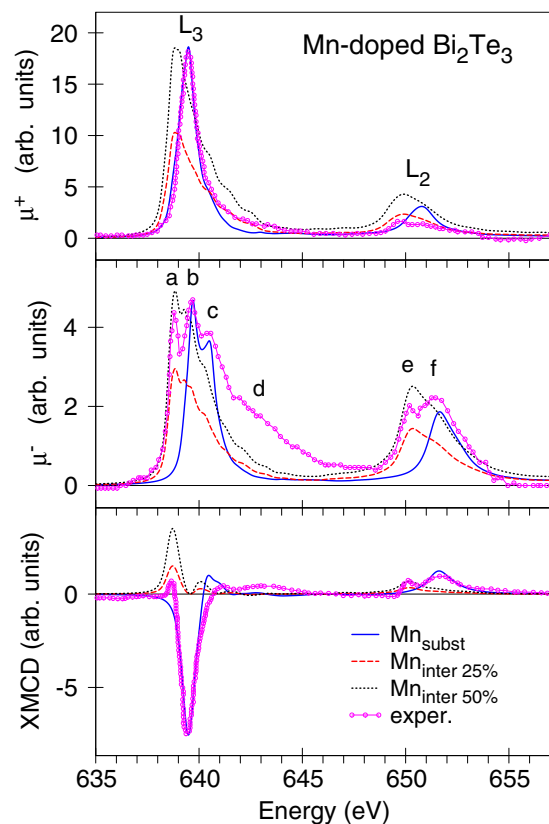


FIG. 5. The x-ray Mn  $L_{2,3}$  absorption spectra (open circles) with normal x-ray incidence for  $\text{Bi}_2\text{Te}_3$  with a Mn coverage of about 0.016 ML measured at 2.5 K in a magnetic field of 6 T applied along the photon beam direction for the left (top) and right (middle) circularly polarized x rays [34] compared with the theoretically calculated spectra for the substitutional Mn ions (full blue curves) and Mn in the van der Waals gap between the QLs (dotted black curves). The lower panel shows the experimental XMCD spectra (open circles) [34] compared with the theoretically calculated spectra for the substitutional Mn ions (full blue curves) and Mn in the van der Waals gap between the QLs (dotted black curves). We also present calculated XAS and XMCD spectra for 25% of Mn ions in the interstitial positions (dashed red curves).

several groups [22,29,34]. Figure 5 presents the experimental XAS and XMCD spectra [34] of Mn-diluted  $\text{Bi}_2\text{Te}_3$  at the Mn  $L_{2,3}$  edges measured at 2.5 K in a magnetic field of 6 T applied along the photon beam direction for the left  $\mu^+$  (top panel) and right  $\mu^-$  (middle panel) circularly polarized x rays together with the spectra calculated in the GGA.

The x-ray absorption spectrum at the Mn  $L_3$  edge for the right circularly polarized x rays  $\mu^-$  (middle panel in Fig. 5) is rather complicated and consists of four major structures: peaks  $a$ ,  $b$ , and  $c$  at 638.6, 639.7, and 640.6 eV, respectively, and a high-energy shoulder  $d$  at 642 eV. The corresponding  $L_2$  XAS has a double peak structure ( $e$  and  $f$  peaks). The x-ray absorption spectrum at the Mn  $L_3$  edge for the left circularly polarized x rays  $\mu^+$  (top panel in Fig. 5) has significantly larger intensity in comparison with the  $\mu^+$  and consists of the major peak at 639.7 eV and a weak low-energy shoulder.

It is well known that as the valence changes from  $\text{Mn}^{2+}$  to  $\text{Mn}^{3+}$  and to  $\text{Mn}^{4+}$  states, the  $L_3$  XAS shows a shift

toward higher energy, and the spectral shape changes with the number of  $3d$  electrons [84]. We found that the valency of the substitutional  $\text{Mn}_{\text{subst}}$  and interstitial  $\text{Mn}_{\text{inter}}$  ions are equal to  $2.5+$  and  $1.7+$ , respectively. Therefore the contributions from the substitutional  $\text{Mn}_{\text{subst}}$  ions with higher ionicity are situated at higher energies. As may be seen from the middle panel of Fig. 5, the calculations with one substitutional  $\text{Mn}_{\text{subst}}$  atom (full blue curve) provide the x-ray absorption intensity only at the peaks  $b$  and  $c$  of  $L_3$  spectrum and peak  $f$  of the  $L_2$  XAS. The full explanation of the spectrum is only possible by taking into account an additional  $\text{Mn}_{\text{inter}}$  ion in the van der Waals gap between the QLs (dotted black curves). The interstitial Mn ions mostly determine the shape of the peaks  $a$  and  $e$  and also contribute to the  $b$  and  $c$  peaks. However, the high-energy shoulder  $d$  is not appeared in our first principles calculations. This might indicate that additional satellite structures may appear due to many-body effects at the high energy tail of the Mn  $L_3$  XAS. This question needs additional theoretical investigation using an appropriate many-body treatment.

The theoretically calculated Mn  $L_{2,3}$  XMCD spectra are in good agreement with the experiment (lower panel in Fig. 5). The XMCD from the substitutional  $\text{Mn}_{\text{subst}}$  atoms (full blue curve) reproduces well the experimental spectrum except of the low energy positive peak at around 638.6 eV at the  $L_3$  edge and fine structure at 650 eV at the  $L_2$  edge, which are due to the  $\text{Mn}_{\text{inter}}$  ions in the van der Waals gap. The theory also does not produce the fine structure corresponding to the high-energy satellite structure  $d$  at around 642 eV. The theory overestimates the intensity of the peak appeared from the  $\text{Mn}_{\text{inter}}$  at around 638.6 eV at the  $L_3$  edge and the fine structure at 650 eV at the  $L_2$  edge. It may be explained by the fact that the calculations presented in Fig. 5 (dotted black curves) have been made for the 50% concentration of the interstitial Mn ions, while the concentration of the interstitial Mn atoms is expected to be less. One would expect strong suppression of the peak with a smaller  $\text{Mn}_{\text{inter}}$  concentration. Indeed, the calculations with 25% of Mn ions in the interstitial positions and 75% of Mn ions in the substitutional positions (dashed red curves in Fig. 5) are in better agreement with the experiment.

It is necessary to distinguish between *homogeneously* mixed-valence compounds and *inhomogeneously* mixed-valence compounds. The homogeneously mixed-valence phenomena appear mostly when all the ions occupy crystallographically equivalent sites and therefore, this is essentially a single ion property where the magnetic ion hybridizes with the sea of the conduction electrons, causing an exchange of the inner electron with the conduction band at the Fermi level. Such effects are expected to arise in systems where two electron configurations corresponding to occupation numbers  $n$  and  $n - 1$  have nearly degenerate energies. So the ground state of a homogeneously mixed valence compound is a quantum mechanical mixture of the both configurations on each ion. Typical compounds exhibiting homogeneously mixed-valence phenomena are rare-earth materials  $\text{TmSe}$  [85],  $\text{SmS}$  (high-pressure golden phase) [86],  $\text{YbB}_{12}$  and  $\text{SmB}_6$  [87],  $\text{EuN}$  [88],  $\text{YbAgCu}_4$  [89],  $\text{YbInCu}_4$  [90], and  $\text{SmRh}_2\text{Si}_2$  [91].

In the case of inhomogeneously or static mixed-valence compounds, rare-earth or transition metal ions with different valency occupy clearly different sites. However, at high temperatures, they become usually homogeneously mixed-valence

semimetals or valence-fluctuating insulators. Their valence electrons are strongly correlated and close to localization, i.e., having a low effective kinetic energy. The valence electrons can hop between the magnetic ions with different valence due to thermal activation (a thermal valence fluctuating state). If the intersite Coulomb repulsion is large enough, it may dominate the kinetic energy and, once the charge-disorder entropy due to hopping is low enough, lead to a charge-ordered transition at a critical temperature  $T_{co}$  below which the valence fluctuation are suppressed. The resulting inhomogeneously mixed-valence state consists of two species of ions with the  $n$  and  $n - 1$  configurations. This transition may be compared to a Wigner crystallization on a lattice [92], and its earliest example is the Verwey transition in magnetite  $\text{Fe}_3\text{O}_4$  [93], although this picture turned out to be too simplified for this compound [94,95]. There are several charge-fluctuating inhomogeneous mixed-valence compounds containing rare-earth and transition metal ions. They are the rare-earth pnictides  $\text{Yb}_4\text{As}_3$  [96],  $\text{Sm}_4\text{Bi}_3$  and  $\text{Eu}_4\text{As}_3$  with the cubic anti- $\text{Th}_3\text{P}_4$  structure and rare-earth chalcogenides  $\text{Sm}_3\text{X}_4$  ( $X = \text{S}, \text{Se}, \text{or Te}$ ) and  $\text{Eu}_3\text{S}_4$  with the  $\text{Th}_3\text{P}_4$  structure [97] and titanium oxide  $\text{Ti}_4\text{O}_7$  [98]. Recently, it was shown that possible oxygen vacancies may be the reason for mixed valency in some complex transition metal oxides such as  $\text{BaFeO}_{3-\delta}$  [99] and  $\text{A}_2\text{CrB}'\text{O}_6$  ( $A = \text{Ca}, \text{Sr}; B' = \text{W}, \text{Re}, \text{and Os}$ ) [100] as well as diluted magnetic semiconductors  $(\text{Zn},\text{V})\text{O}$  [101] and  $(\text{Zn},\text{Co})\text{O}$  [102].

The mixed valency in Mn-doped topological insulators  $\text{Bi}_2\text{Se}_3$  and  $\text{Bi}_2\text{Te}_3$  appears due to the different crystallographic positions of the substitutional and interstitial Mn ions. Both substitutional and interstitial ions have six Te neighbors (atomic configuration  $4d^{10}5s^25p^4$ ) with approximately the same interatomic distances, however, they have different number of Bi neighbor ions (atomic configuration  $5d^{10}6s^26p^3$ ): the substitutional  $\text{Mn}_{\text{subst}}$  ion possesses three Bi neighbors but the interstitial  $\text{Mn}_{\text{inter}}$  ion has only two Bi neighbors. As a result, the valencies were found to be equal to  $2.5+$  ( $d^{4.5}$ ) and  $1.7+$  ( $d^{5.3}$ ) for the  $\text{Mn}_{\text{subst}}$  and  $\text{Mn}_{\text{inter}}$  ions, respectively. We can conclude that these Mn-doped topological insulators belong to the inhomogeneously or static mixed-valence compounds of charge transfer type. Besides, from the total energy calculations, we found that the magnetic moment of Mn ions in the van der Waals gap orders antiferromagnetically to the magnetic moment of the substitutional Mn ions. This conclusion is supported by the XMCD measurements where the peaks  $a$  and  $b$  in Fig. 5 (lower panel), which are originated from the interstitial and substitutional Mn ions, respectively, have opposite signs. We can conclude that the incorporation of Mn ions in the van der Waals gap changes the magnetic ordering in the system from the ferromagnetic to the ferrimagnetic one. We found that the concentration of Mn ions in the interstitial positions is around 25%.

Figure 6 presents experimental XAS and XMCD spectra [22] of Mn-diluted  $\text{Bi}_2\text{Se}_3$  at the Mn  $L_{2,3}$  edges measured at 2.5 K in a magnetic field of 2 T applied along the photon beam direction for the left  $\mu^+$  (top panel) and right  $\mu^-$  (middle panel) circularly polarized x rays together with the spectra calculated in the GGA. The x-ray absorption spectra at the Mn  $L_3$  edge for the right circularly polarized x rays also consist of four major peaks  $a$ ,  $b$ , and  $c$  and a high-energy shoulder  $d$ . The substitutional  $\text{Mn}_{\text{subst}}$  atoms (full blue curve) provide

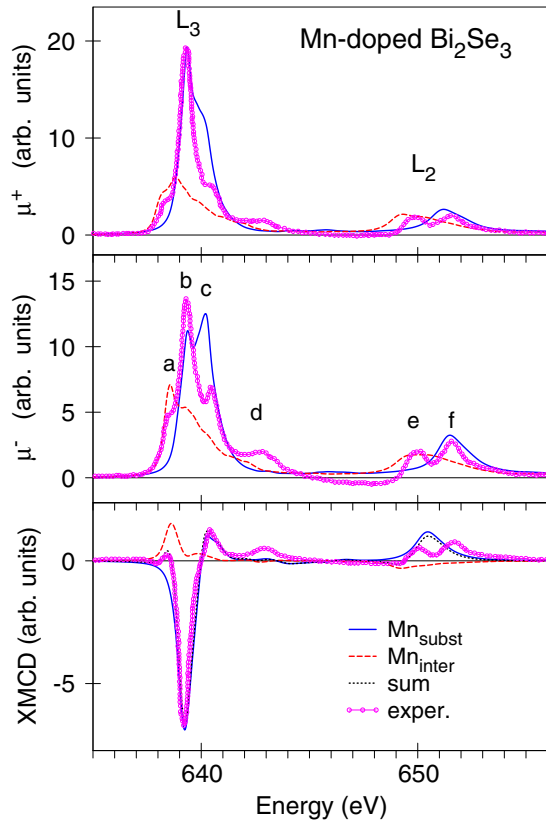


FIG. 6. The x-ray  $L_{2,3}$  absorption spectra (open magenta circles) for a 7.5 at. % Mn-doped  $\text{Bi}_2\text{Se}_3$  sample measured at 2.5 K in a magnetic field of 2 T applied along the photon beam direction for the left (top panel) and right (middle panel) circularly polarized x rays [22] compared with the theoretically calculated spectra for the substitutional Mn ions (full blue curves) and Mn in the van der Waals gap between the QLs (dashed red curves). The lower panel shows the experimental XMCD spectra (open magenta circles) [22] compared with the theoretically calculated spectra for the substitutional Mn ions (full blue curves) and Mn in the van der Waals gap (dashed red curves). The shown XMCD spectra are for the 25% of Mn ions in the interstitial positions and 75% of Mn ions in the substitutional positions.

the x-ray absorption intensity to the peaks  $b$  and  $c$  of the  $L_3$  spectrum and the peak  $f$  of the  $L_2$  XAS. The interstitial Mn ions mostly determine the shape of the peaks  $a$  and  $e$  (dashed red curve) but also contribute to the  $b$  and  $c$  peaks. The high-energy shoulder  $d$  is also not described by one-electron theory. The x-ray absorption spectrum at the Mn  $L_3$  edge for the left circularly polarized x rays  $\mu^+$  (top panel in Fig. 6) has significantly larger intensity in comparison with the  $\mu^-$  and consists of the major peak at 639.7 eV, a weak low-energy shoulder, and two high-energy fine structures at 640.6 and 643 eV. The former high-energy peak is described by the theory, however, the last peak corresponding to the peak  $d$  for the right circularly polarized x rays is absent in the theoretical calculations.

The theoretically calculated Mn  $L_{2,3}$  XMCD spectra are also in good agreement with the experiment (lower panel in Fig. 6). The XMCD from the substitutional  $\text{Mn}_{\text{subst}}$  atoms (full blue curve) reproduces well the experimental spectrum except

of the low-energy positive peak at around 638.6 eV at the  $L_3$  edge and fine structure at 650 eV at the  $L_2$  edge, which are due to the  $\text{Mn}_{\text{inter}}$  ions in the van der Waals gap. We also found that the best agreement between the theory and the experiment can be achieved with 25% of Mn ions in the interstitial positions and 75% of Mn ions in the substitutional positions.

We found only minor influence of the structure relaxation on the partial DOS in close vicinity of the Fermi level ( $\pm 0.1$  eV), further away from the Fermi level the PDOSs did not change. The lattice optimization also did not affect the XAS and XMCD spectra which are extended in a wide energy interval. We investigate also the core-hole effect in the final state using the supercell approximation where the excited atom is formally treated as an impurity. We found that the core-hole interactions slightly improve the agreement between theoretically calculated and experimentally measured Mn  $L_{2,3}$  XASs.

### B. Mn $K$ XAS and XMCD spectra

The XAS and XMCD spectra in metals and alloys at the  $K$  edge in which the  $1s$  core electrons are excited to  $p$  states through the dipole transitions are quite important. They are sensitive to the electronic states at neighboring sites because of the delocalized nature of valence  $p$  states. Since dipole allowed transitions dominate the absorption spectrum for unpolarized radiation, the absorption coefficient reflects primarily the DOS of unoccupied  $4p$ -like  $N_p(E)$  above the Fermi level. The exchange splitting of the initial  $1s$  core state is extremely small, therefore, only the exchange and spin-orbit splitting of the final  $4p$  states is responsible for the observed dichroism at the  $K$  edge. For this reason the dichroism is found to be relatively small.

Figure 7 presents the theoretically calculated XAS (top panel) and the XMCD (lower panel) spectra for the substitutional  $\text{Mn}_{\text{subst}}$  ions (full blue curves) and the  $\text{Mn}_{\text{inter}}$  ions in the van der Waals gap (dashed red curves) at the Mn  $K$  edge of Mn-doped  $\text{Bi}_2\text{Te}_3$  TI. The Mn  $K$  XASs are spread up to 50 eV above the threshold and quite structured, showing well defined features. The XASs for the  $\text{Mn}_{\text{subst}}$  and  $\text{Mn}_{\text{inter}}$  ions have similar shapes with different relative intensities of fine structures. The  $\text{Mn}_{\text{subst}}$  spectrum has a more intensive peak at 7–9 eV in comparison with the  $\text{Mn}_{\text{inter}}$  spectrum. The XMCD spectra at the Mn  $K$  edge are also structured, showing well defined features and consist of several positive and negative peaks. The difference between the  $\text{Mn}_{\text{subst}}$  and  $\text{Mn}_{\text{inter}}$  XMCD spectra is more pronounced in comparison with the corresponding XAS spectra (lower panel in Fig. 7). The core-hole effect was found to be less significant for the Mn  $K$  than for the Mn  $L_{2,3}$  XASs. The experimental measurements of the XAS and XMCD spectra at the Mn  $K$  edge are highly desirable.

### C. Mn XES spectra

Figure 8 presents the theoretically calculated x-ray emission (XES) spectra for the substitutional  $\text{Mn}_{\text{subst}}$  ions (full blue curves) and  $\text{Mn}_{\text{inter}}$  in the van der Waals gap (dashed red curves) spectra at the Mn  $L_3$  (top panel) and Mn  $K$  (bottom panel) edges in the Mn-doped  $\text{Bi}_2\text{Te}_3$  TI. The Mn  $L_3$  XESs for

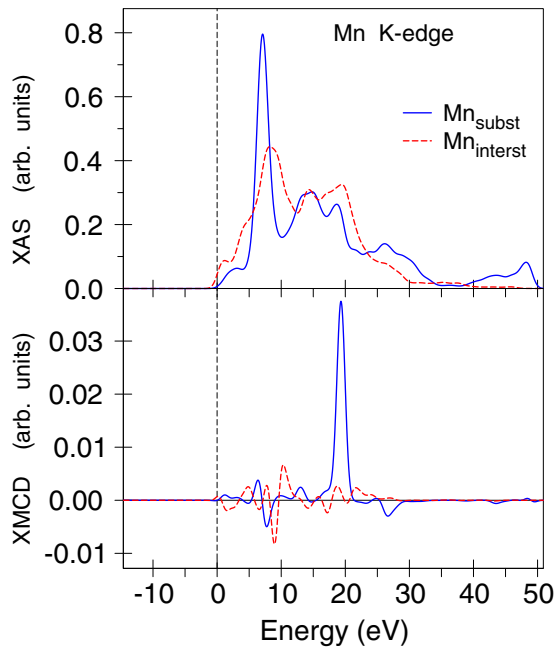


FIG. 7. The theoretically calculated x-ray  $K$  absorption spectra (top) and the XMCD spectra for the substitutional  $\text{Mn}_{\text{subst}}$  ions (full blue curves) and  $\text{Mn}_{\text{interst}}$  in the van der Waals gap between the QLs (dashed red curves) in the Mn-doped  $\text{Bi}_2\text{Te}_3$ .

the  $\text{Mn}_{\text{subst}}$  and  $\text{Mn}_{\text{interst}}$  ions possess similar structures with the major peak at  $-1$  eV. The  $\text{Mn}_{\text{interst}}$   $L_3$  XES has an additional low-energy fine structure at  $-4$  eV and high-energy shoulder in the close vicinity of the  $L_3$  threshold. The last structure appears due to the existence of a narrow  $3d$  peak in the close vicinity of the Fermi energy at  $-0.2$  eV for the  $\text{Mn}_{\text{interst}}$  ions (see lower panel of Fig. 4).

The Mn  $K$  XESs possess quite different shape for the  $\text{Mn}_{\text{subst}}$  and  $\text{Mn}_{\text{interst}}$  ions (lower panel of Fig. 8) due to

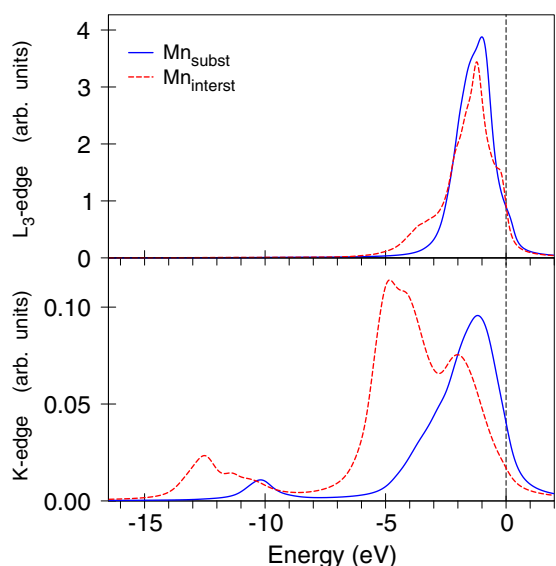


FIG. 8. The theoretically calculated x-ray emission spectra at the  $L_3$  (top) and  $K$  (bottom) edges for the substitutional Mn ions (full blue curves) and Mn in the van der Waals gap between the QLs (dashed red curves) in the Mn-doped  $\text{Bi}_2\text{Te}_3$  TI.

significantly different energy distribution of the partial DOSs of occupied  $4p$ -like states below the Fermi level due to a different degree of the hybridization between Mn  $3d$  and the Te and Bi  $p$  states for these two types of Mn ions. The width of the  $\text{Mn}_{\text{interst}}$   $K$  XES is much larger than the corresponding XES at the  $\text{Mn}_{\text{subst}}$  site. The XES spectrum for the  $\text{Mn}_{\text{subst}}$  ions possesses one major peak at  $-1$  eV with a small low-energy peak at  $-10$  eV. The  $\text{Mn}_{\text{interst}}$   $K$  XES spectrum has three peaks at  $-2$ ,  $-5$ , and  $-12.5$  eV. We also investigated the effect of the electric quadrupole  $E$  transitions ( $3d \rightarrow 1s$  transitions) on the shape of the Mn  $K$  x-ray emission spectra and found only minor influence of these transitions: less than 2% of quadrupole transitions contribute to the intensity of the spectra.

The Mn  $K$  x-ray emission spectroscopy can be a useful tool for the estimation of the relative concentrations of the  $\text{Mn}_{\text{subst}}$  and  $\text{Mn}_{\text{interst}}$  ions in the  $\text{Bi}_2\text{Te}(\text{Se})_3$  matrix. The experimental measurements of the x-ray emission spectra at the Mn  $K$  and  $L_{2,3}$  edges are highly desirable.

## V. CONCLUSIONS

The electronic structure of surface states was investigated for the crystal structure of the  $\text{Bi}_2\text{Se}_3$  and  $\text{Bi}_2\text{Te}_3$  (111) thin films with the thickness of six QLs with one quintuple replaced by empty spheres. In the fully relativistic Dirac approximation, two chiral surface states connect the conduction and valence bands forming a single Dirac-type contact at the  $\Gamma$  point aligned with the Fermi energy in  $\text{Bi}_2\text{Se}_3$ . The gapless surface states have almost linear energy dependence near the Dirac point. A linear band structure in 2D leads to linear density of states. This type of DOS can be easily measured by the low-temperature scanning tunneling spectroscopy, which will provide an indirect method to probe the existence of linear surface states. We found that when the Fermi level is close to the Dirac point in  $\text{Bi}_2\text{Se}_3$  the corresponding Fermi surface is nearly a perfect circle, while if the Fermi level is away from the Dirac point the properties of the surface states are significantly affected by the bulk states and thus satisfy a hexagonal symmetry. There is a crucial detail that distinguishes  $\text{Bi}_2\text{Te}_3$  from  $\text{Bi}_2\text{Se}_3$ : in  $\text{Bi}_2\text{Se}_3$  the DP is located a few hundred meV below the Fermi energy  $E_F$ , while the DP of the  $\text{Bi}_2\text{Te}_3$  is situated deeply below the  $E_F$  and the valence-band maximum.

In this work, we studied the electronic structure and x-ray magnetic circular dichroism of Mn-doped  $\text{Bi}_2\text{Se}_3$  and  $\text{Bi}_2\text{Te}_3$  within a DFT-GGA approach in the frame of the fully relativistic spin-polarized Dirac LMTO band-structure method. The complex fine structure of the Mn  $L_{2,3}$  XAS in Mn-doped  $\text{Bi}_2\text{Se}_3$  and  $\text{Bi}_2\text{Te}_3$  was found to be not compatible with a pure  $\text{Mn}^{3+}$  valency state. Its interpretation demands mixed valent states. Mn-doped  $\text{Bi}_2(\text{Se}, \text{Te})_3$  may contain both the substitutional  $\text{Mn}_{\text{subst}}$  ions and the  $\text{Mn}_{\text{interst}}$  ions in the van der Waals gap between the QLs. The mixed valency in Mn-doped topological insulators  $\text{Bi}_2\text{Se}_3$  and  $\text{Bi}_2\text{Te}_3$  appears due to the different crystallographic positions of the substitutional and interstitial Mn ions. Both substitutional and interstitial ions have six Te neighbors with approximately the same interatomic distances, however, they have different number of Bi neighbor ions: the substitutional  $\text{Mn}_{\text{subst}}$  ion possesses three Bi neighbors but the interstitial  $\text{Mn}_{\text{interst}}$  ion has only two Bi neighbors. As a result, the valencies were found to

be equal to  $2.5+$  ( $d^{4.5}$ ) and  $1.7+$  ( $d^{5.3}$ ) for the  $\text{Mn}_{\text{subst}}$  and  $\text{Mn}_{\text{inter}}$  ions, respectively. We can conclude that these Mn-doped topological insulators belong to the inhomogeneously or static mixed-valence compounds of charge transfer type. Besides, from the total energy calculations, we found that the magnetic moment of Mn ions in the van der Waals gap orders antiferromagnetically to the magnetic moment of the substitutional Mn ions. This conclusion is supported by XMCD measurements where the peaks  $a$  and  $b$  in Fig. 5 (lower panel), which are originated from the interstitial and substitutional Mn ions, respectively, have opposite signs. We can conclude that the incorporation of Mn ions in the van der Waals gap changes the magnetic ordering in the system from the ferromagnetic to the ferrimagnetic one. We found that the concentration of Mn ions in the interstitial positions is around 25%.

We also present the theoretically calculated XAS and XMCD spectra as well as x-ray emission spectra at the Mn

$K$  edges in the Mn-doped  $\text{Bi}_2\text{Te}_3$ . These spectra possess quite different shapes for the  $\text{Mn}_{\text{subst}}$  and  $\text{Mn}_{\text{inter}}$  ions due to significantly different energy distribution of the partial DOSs of  $4p$ -like states. The Mn  $K$  x-ray emission and absorption spectroscopy can be a useful tool for the estimation of the relative concentrations of the  $\text{Mn}_{\text{subst}}$  and  $\text{Mn}_{\text{inter}}$  ions in the  $\text{Bi}_2\text{Te}(\text{Se})_3$  matrix. The experimental measurements of the XAS and XMCD spectra as well as x-ray emission spectra at the Mn  $K$  edge in the Mn-doped TI's are highly desired.

#### ACKNOWLEDGMENTS

V.N.A. gratefully acknowledges the hospitality at the Faculty of Mathematics and Informatics of the University of Bialystok and Max-Planck Institute for Microstructure Physics in Halle.

- 
- [1] X.-L. Qi and S.-C. Zhang, *Phys. Today* **63**(1), 33 (2010).
- [2] P. Roushan, J. Seo, C. V. Parker, Y. S. Hor, D. Hsieh, D. Qian, A. Richardella, M. Z. Hasan, R. J. Cava, and A. Yazdani, *Nature (London)* **460**, 1106 (2009).
- [3] H. Zhang, C.-X. Liu, X.-L. Qi, X. Dai, Z. Fang, and S.-C. Zhang, *Nat. Phys.* **5**, 438 (2009).
- [4] Y. Xia, D. Qian, D. Hsieh, L. Wray, A. Pal, H. Lin, A. Bansil, D. Grauer, Y. S. Hor, R. J. Cava *et al.*, *Nat. Phys.* **5**, 398 (2009).
- [5] Y. L. Chen, J. G. Analytis, J. H. Chu, Z. K. Liu, S. K. Mo, X. L. Qi, H. J. Zhang, D. H. Lu, X. Dai, Z. Fang *et al.*, *Science* **325**, 178 (2009).
- [6] S. R. Park, W. S. Jung, C. Kim, D. J. Song, C. Kim, S. Kimura, K. D. Lee, and N. Hur, *Phys. Rev. B* **81**, 041405(R) (2010).
- [7] C.-X. Liu, X.-L. Qi, H. J. Zhang, X. Dai, Z. Fang, and S.-C. Zhang, *Phys. Rev. B* **82**, 045122 (2010).
- [8] L. Fu and C. L. Kane, *Phys. Rev. Lett.* **100**, 096407 (2008).
- [9] K. J. Plucinski, W. Gruhn, I. V. Kityk, W. Imiolek, H. Kaddouri, and S. Benet, *Opt. Commun.* **204**, 355 (2002).
- [10] M. Z. Hasan and C. L. Kane, *Rev. Mod. Phys.* **82**, 3045 (2010).
- [11] X.-L. Qi and S.-C. Zhang, *Rev. Mod. Phys.* **83**, 1057 (2011).
- [12] Y. Ando, *J. Phys. Soc. Jpn.* **82**, 102001 (2013).
- [13] T. O. Wehling, A. Black-Schafferc, and A. Balatsky, *Adv. Phys.* **63**, 1 (2014).
- [14] A. Bansi, L. H, and T. Das, *Rev. Mod. Phys.* **88**, 021004 (2016).
- [15] C.-Z. Chang, J. Zhang, M. Liu, Z. Z. X. Feng, K. Li, L.-L. Wang, X. Chen, X. Dai, Z. Fang, X.-L. Qi *et al.*, *Adv. Mater.* **25**, 1065 (2013).
- [16] W.-K. Tse and A. H. MacDonald, *Phys. Rev. Lett.* **105**, 057401 (2010).
- [17] C.-Z. Chang, J. Zhang, X. Feng, J. Shen, Z. Zhang, M. Guo, K. Li, Y. Ou, P. Wei, L.-L. Wang *et al.*, *Science* **340**, 167 (2013).
- [18] R. Yu, W. Zhang, H.-J. Zhang, S.-C. Zhang, X. Dai, and Z. F., *Science* **329**, 61 (2010).
- [19] Y. J. Chien, Ph.D. thesis, University Michigan, 2007.
- [20] J. S. Dyck, P. Hajek, P. Lostak, and C. Uher, *Phys. Rev. B* **65**, 115212 (2002).
- [21] Y. S. Hor, P. Roushan, H. Beidenkopf, J. Seo, D. Qu, J. G. Checkelsky, L. A. Wray, D. Hsieh, Y. Xia, S.-Y. Xu *et al.*, *Phys. Rev. B* **81**, 195203 (2010).
- [22] L. J. Collins-McIntyre, M. D. Watson, A. A. Baker, S. L. Zhang, A. I. Coldea, S. E. Harrison, A. Pushp, A. J. Kellock, S. S. P. Parkin, G. van der Laan *et al.*, *AIP Adv.* **4**, 127136 (2014).
- [23] L. J. Collins-McIntyre, S. E. Harrison, P. Schoenherr, N. J. Steinke, C. J. Kinane, T. R. Charlton, D. Alba-Veneroa, A. Pushp, A. J. Kellock, S. S. P. Parkin *et al.*, *Europhys. Lett.* **107**, 57009 (2014).
- [24] A. I. Figueroa, G. van der Laan, L. J. Collins-McIntyre, S. L. Zhang, A. A. Baker, S. E. Harrison, P. Schonherr, G. Cibin, and T. Hesjedal, *Phys. Rev. B* **90**, 134402 (2014).
- [25] X. Kou, S.-T. Guo, Y. Fan, L. Pan, M. Lang, Y. Jiang, Q. Shao, T. Nie, K. Murata, J. Tang *et al.*, *Phys. Rev. Lett.* **113**, 137201 (2014).
- [26] J. G. Checkelsky, R. Yoshimi, A. Tsukazaki, K. S. Takahashi, Y. Kozuka, J. Falson, M. Kawasaki, and Y. Tokura, *Nat. Phys.* **10**, 731 (2014).
- [27] Y. J. Chien, Transition metal-doped  $\text{Sb}_2\text{Te}_3$  and  $\text{Bi}_2\text{Te}_3$  diluted magnetic semiconductors, Ph.D. dissertation, University Michigan, Michigan, 2007.
- [28] C.-Z. Chang, W. Zhao, D. Y. Kim, H. Zhang, B. A. Assaf, D. Heiman, S.-C. Zhang, C. Liu, M. H. W. Chan, and J. S. Moodera, *Nat. Mater.* **14**, 473 (2015).
- [29] M. D. Watson, L. J. Collins-McIntyre, L. R. Shelford, A. I. Coldea, D. Prabhakaran, S. C. Speller, T. Mousavi, C. R. M. Grovenor, Z. Salman, S. R. Giblin *et al.*, *New J. Phys.* **15**, 103016 (2013).
- [30] C. Niu, Y. Dai, M. Guo, W. Wei, Y. Ma, and B. Huang, *Appl. Phys. Lett.* **98**, 252502 (2011).
- [31] J. Henk, A. Ernst, S. V. Ereameev, E. V. Chulkov, I. V. Maznichenko, and I. Mertig, *Phys. Rev. Lett.* **108**, 206801 (2012).
- [32] P. Larson and W. R. L. Lambrecht, *Phys. Rev. B* **78**, 195207 (2008).
- [33] J.-M. Zhang, W. Zhu, Y. Zhang, D. Xiao, and Y. Yao, *Phys. Rev. Lett.* **109**, 266405 (2012).
- [34] P. Sessi, P. Rümman, T. Bathon, A. Barla, K. A. Kokh, O. E. Tereshchenko, K. Fauth, S. K. Mahatha, M. A. Valbuena, S. Godey *et al.*, *Phys. Rev. B* **94**, 075137 (2016).

- [35] E. M. Black, L. Conwell, L. Seigle, and C. W. Spencer, *J. Phys. Chem. Solids* **2**, 240 (1957).
- [36] A. D. LaForge, A. Frenzel, B. C. Pursley, T. Lin, X. Liu, J. Shi, and D. N. Basov, *Phys. Rev. B* **81**, 125120 (2010).
- [37] G. Y. Guo, H. Ebert, W. M. Temmerman, and P. J. Durham, *Phys. Rev. B* **50**, 3861 (1994).
- [38] V. N. Antonov, A. I. Bagljkuk, A. Y. Perlov, V. V. Nemoshkalenko, V. N. Antonov, O. K. Andersen, and O. Jepsen, *Fiz. Nizk. Temp.* **19**, 689 (1993) [*Low Temp. Phys.* **19**, 494 (1993)].
- [39] V. Antonov, B. Harmon, and A. Yaresko, *Electronic Structure and Magneto-Optical Properties of Solids* (Kluwer, Dordrecht, 2004).
- [40] E. Arola, M. Horne, P. Strange, H. Winter, Z. Szotek, and W. M. Temmerman, *Phys. Rev. B* **70**, 235127 (2004).
- [41] B. T. Thole and G. van der Laan, *Phys. Rev. B* **38**, 3158 (1988).
- [42] B. T. Thole, P. Carra, F. Sette, and G. van der Laan, *Phys. Rev. Lett.* **68**, 1943 (1992).
- [43] P. Carra, B. T. Thole, M. Altarelli, and X. Wang, *Phys. Rev. Lett.* **70**, 694 (1993).
- [44] B. T. Thole and G. van der Laan, *Phys. Rev. Lett.* **70**, 2499 (1993).
- [45] G. van der Laan and B. T. Thole, *Phys. Rev. B* **53**, 14458 (1996).
- [46] G. van der Laan, *Phys. Rev. B* **57**, 112 (1998).
- [47] V. N. Antonov, O. Jepsen, A. N. Yaresko, and A. P. Shpak, *J. Appl. Phys.* **100**, 043711 (2006).
- [48] V. N. Antonov, B. N. Harmon, A. N. Yaresko, and A. P. Shpak, *Phys. Rev. B* **75**, 184422 (2007).
- [49] V. N. Antonov, A. N. Yaresko, and O. Jepsen, *Phys. Rev. B* **81**, 075209 (2010).
- [50] V. P. Antropov, V. N. Antonov, L. V. Bekenov, A. Kutepov, and G. Kotliar, *Phys. Rev. B* **90**, 054404 (2014).
- [51] O. K. Andersen, *Phys. Rev. B* **12**, 3060 (1975).
- [52] A. Y. Perlov, A. N. Yaresko, and V. N. Antonov, PY-LMTO, A Spin-polarized Relativistic Linear Muffin-tin Orbitals Package for Electronic Structure Calculations (1995) (unpublished).
- [53] V. V. Nemoshkalenko, A. E. Krasovskii, V. N. Antonov, V. N. Antonov, U. Fleck, H. Wonn, and P. Ziesche, *Phys. Status Solidi B* **120**, 283 (1983).
- [54] A. H. MacDonald, W. E. Pickett, and D. D. Koelling, *J. Phys. C* **13**, 2675 (1980).
- [55] J. P. Perdew, K. Burke, and M. Ernzerhof, *Phys. Rev. Lett.* **77**, 3865 (1996).
- [56] J. P. Perdew, K. Burke, and M. Ernzerhof, *Phys. Rev. Lett.* **78**, 1396 (1997).
- [57] P. E. Blöchl, O. Jepsen, and O. K. Andersen, *Phys. Rev. B* **49**, 16223 (1994).
- [58] T. Zhang, P. Cheng, X. Chen, J.-F. Jia, X. Ma, K. He, L. Wang, H. Zhang, X. Dai, Z. Fang *et al.*, *Phys. Rev. Lett.* **103**, 266803 (2009).
- [59] R. W. Wyckoff, *Crystal Structures* (Wiley, New York, 1964), Vol. 2.
- [60] A. N. Mansour, W. Wong-Ng, Q. Huang, W. Tang, A. Thompson, and J. Sharp, *J. Appl. Phys.* **116**, 083513 (2014).
- [61] I. Vobornik, U. Manju, J. Fujii, F. Borgatti, P. Torelli, D. Krizmancic, Y. S. Hor, R. J. Cava, and G. Panaccione, *Nano Lett.* **11**, 4079 (2011).
- [62] P. E. Blöchl, *Phys. Rev. B* **50**, 17953 (1994).
- [63] G. Kresse and D. Joubert, *Phys. Rev. B* **59**, 1758 (1999).
- [64] J. L. Campbell and T. Parr, *At. Data Nucl. Data Tables* **77**, 1 (2001).
- [65] J. Slater, *The Self-Consistent Field Methods for Molecules and Solids* (McGraw-Hill, New York, 1974).
- [66] I. Tanaka and H. Adachi, *Phys. Rev. B* **54**, 4604 (1996).
- [67] M. M. Disko, J. C. H. Spence, O. F. Sankey, and D. Saldin, *Phys. Rev. B* **33**, 5642 (1986).
- [68] K. Lie, R. Brydson, and H. Davock, *Phys. Rev. B* **59**, 5361 (1999).
- [69] K. Lie, R. Hoier, and R. Brydson, *Phys. Rev. B* **61**, 1786 (2000).
- [70] T. Mizoguchi, I. Tanaka, S. Yoshioka, M. Kunisu, T. Yamamoto, and W. Y. Ching, *Phys. Rev. B* **70**, 045103 (2004).
- [71] S. Nufer, T. Gemming, C. Elsässer, S. Köstlemer, and M. Rühle, *Ultramicroscopy* **86**, 339 (2001).
- [72] S.-D. Mo and W. Y. Ching, *Phys. Rev. B* **62**, 7901 (2000).
- [73] S.-D. Mo and W. Y. Ching, *Appl. Phys. Lett.* **78**, 3809 (2001).
- [74] Y.-N. Xu, Y. Chen, S.-D. Mo, and W. Y. Ching, *Phys. Rev. B* **65**, 235105 (2002).
- [75] W.-Y. Ching, S.-D. Mo, and Y. Chen, *J. Am. Ceram. Soc.* **85**, 11 (2002).
- [76] C.-X. Liu, H. J. Zhang, B. Yan, X.-L. Qi, T. Frauenheim, X. Dai, Z. Fang, and S.-C. Zhang, *Phys. Rev. B* **81**, 041307(R) (2010).
- [77] O. V. Yazyev, J. E. Moore, and S. G. Louie, *Phys. Rev. Lett.* **105**, 266806 (2010).
- [78] P. Rakyta, B. Ujfalussy, and L. Szunyogh, *New J. Phys.* **17**, 123011 (2015).
- [79] T. Förster, P. Krüger, and M. Rohlfing, *Phys. Rev. B* **92**, 201404(R) (2015).
- [80] T. Förster, P. Krüger, and M. Rohlfing, *Phys. Rev. B* **93**, 205442 (2016).
- [81] Y. Zhang, K. He, C.-Z. Chang, C.-L. Song, L.-L. Wang, X. Chen, J.-F. Jia, Z. Fang, X. Dai, W.-Y. Shan *et al.*, *Nat. Phys.* **6**, 584 (2010).
- [82] H. M. Benia, C. Lin, K. Kern, and C. R. Ast, *Phys. Rev. Lett.* **107**, 177602 (2011).
- [83] M. Bianchi, R. C. Hatch, D. Guan, T. Planke, J. Mi, and B. B. I. P. Hofmann, *Semicond. Sci. Technol.* **27**, 124001 (2012).
- [84] F. M. F. de Groot, J. C. Fuggle, B. T. Thole, and G. A. Sawatzky, *Phys. Rev. B* **42**, 5459 (1990).
- [85] V. N. Antonov, B. N. Harmon, and A. N. Yaresko, *Phys. Rev. B* **63**, 205112 (2001).
- [86] V. N. Antonov, B. N. Harmon, and A. N. Yaresko, *Phys. Rev. B* **66**, 165208 (2002).
- [87] V. N. Antonov, B. N. Harmon, and A. N. Yaresko, *Phys. Rev. B* **66**, 165209 (2002).
- [88] B. J. Ruck, H. J. Trodahl, J. H. Richter, J. C. Cezar, F. Wilhelm, A. Rogalev, V. N. Antonov, B. D. Le, and C. Meyer, *Phys. Rev. B* **83**, 174404 (2011).
- [89] V. N. Antonov, L. V. Bekenov, and V. P. Antropov, *Phys. Rev. B* **89**, 165110 (2014).
- [90] V. N. Antonov, M. Galli, F. Marabelli, A. N. Yaresko, A. Y. Perlov, and E. Bauer, *Phys. Rev. B* **62**, 1742 (2000).
- [91] A. Chikina, A. Generalov, K. Kummer, M. Gttler, V. N. Antonov, Y. Kucherenko, K. Kliemt, C. Krellner, S. Danzenbcher, T. Kim *et al.*, *Phys. Rev. B* **95**, 155127 (2017).

- [92] P. Fulde, *Ann. Phys.* **509**, 178 (1997).
- [93] E. J. Verwey and P. Haayman, *Physica* **8**, 979 (1941).
- [94] V. N. Antonov, B. N. Harmon, V. P. Antropov, A. Y. Perlov, and A. N. Yaresko, *Phys. Rev. B* **64**, 134410 (2001).
- [95] I. Leonov, A. N. Yaresko, V. N. Antonov, M. A. Korotin, and V. I. Anisimov, *Phys. Rev. Lett.* **93**, 146404 (2004).
- [96] V. N. Antonov, A. N. Yaresko, A. Y. Perlov, P. Thalmeier, P. Fulde, P. M. Oppeneer, and H. Eschrig, *Phys. Rev. B* **58**, 9752 (1998).
- [97] V. N. Antonov, B. N. Harmon, and A. N. Yaresko, *Phys. Rev. B* **72**, 085119 (2005).
- [98] I. Leonov, A. N. Yaresko, V. N. Antonov, U. Schwingenschlogl, V. Eyert, and V. I. Anisimov, *J. Phys.: Condens. Matter* **18**, 10955 (2006).
- [99] I. V. Maznichenko, S. Ostanin, L. V. Bekenov, V. N. Antonov, I. Mertig, and A. Ernst, *Phys. Rev. B* **93**, 024411 (2016).
- [100] V. N. Antonov and L. V. Bekenov, *Low Temp. Phys.* **43**, 578 (2017).
- [101] L. V. Bekenov, V. N. Antonov, S. Ostanin, A. N. Yaresko, I. V. Maznichenko, W. Hergert, I. Mertig, and A. Ernst, *Phys. Rev. B* **84**, 134421 (2011).
- [102] V. N. Antonov, L. V. Bekenov, O. Jepsen, D. V. Mazur, and L. P. Germash, *J. Appl. Phys.* **111**, 073702 (2012).